20th International Symposium on Application of Laser and Imaging Techniques to Fluid Mechanics • LISBON | PORTUGAL • JULY 11-14, 2022

Characterization of Shock Buffet on a Supercritical 2D Airfoil in Transonic Flow

C. J. Schauerte[1,*], A.-M. Schreyer[1]
1: Institute of Aerodynamics, RWTH Aachen University, Germany
*Corresponding author: c.schauerte@aia.rwth-aachen.de

Keywords: Transonic buffet, Supercritical airfoil, Shock-wave/boundary layer interaction, Experimental aerodynamics, Focusing schlieren, PIV processing

ABSTRACT

The transonic flow over the supercritical OAT15A airfoil is investigated experimentally. Using time-resolved focusing schlieren sequences, we extracted the temporal evolution of the chordwise shock location for a wide range of combinations of Mach number and angle of attack. Based on this data, we identified the conditions for most pronounced buffet behavior. Key parameters characterizing this operating condition are presented and quantified in terms of the shock amplitude, its variation over multiple buffet cycles, and the associated frequency of the periodic shock oscillation. Fully-established buffet is identified at a Mach number of $M_\infty = 0.72$ and an angle of attack of $\alpha = 5$ °. It is demonstrated that these operating conditions are characterized by a quasi-sinusoidal shock oscillation at a distinct frequency of 113 Hz, in good agreement with previous studies. This analysis reveals that the harmonic shock oscillation spanning a range of about 16.5 % of the airfoil chord is accompanied by a coupled large-scale variation of the global flow topology. Both instantaneous and mean velocity components in the chordwise and vertical directions are discussed for representative phases of the buffet cycle. Instantaneous vector fields provide insight into the flow organization throughout the buffet cycle and allow to identify the streamwise distance traveled by the shock wave within a full cycle. We can thus precisely capture the state of the shock wave, and quantify the evolution of the shock-induced separation and the size of the turbulent wake. Severe variations of the flow topology are induced by the large-scale up-stream and downstream shock displacement. The results show that incidents of massive flow separation are observed for shock positions being close to the upstream limit, and more general, that the wake influence is more pronounced when induced by an upstream traveling shock wave. Phase-averaged velocity profiles at significant locations along the airfoil suction side complement this analysis. Characteristic sets of velocity profiles are discussed in detail that allow to uniquely describe the development of the flow in each phase of the buffet cycle. Detailed contours and pro-files of both velocity and Reynolds shear stress contributions across the wake region highlight the strong downstream influence the shock-induced turbulent wake. Phases of severe flow separation result in reverse flow persisting until the trailing edge which further substantiates the induced momentum deficit.

1. Introduction

The transonic flight regime is often characterized by the occurrence of local supersonic regions on the suction side of airfoils and wings, which are terminated by a shock wave (McDevitt & Okuno, 1985), and shock-induced flow separation may span the entire region from the shock to the trailing edge (Molton et al., 2013). For certain combinations of Mach number, Reynolds number, and angle of attack, the transonic flow about the airfoil becomes unsteady, with the compression shock and separated boundary layer carrying out periodic oscillations (McDevitt & Okuno, 1985). The resulting complex shock-wave/boundary-layer interaction involves major parts of the flow field (Jacquin et al., 2009) and is typically referred to as transonic buffet. The occurrence of transonic buffet is, inter alia, associated with a highly unsteady flow field (Molton et al., 2013), severe oscillations of the lift coefficient (Crouch et al., 2008), and fluctuating aerodynamic forces on the aircraft (Benoit & Legrain, 1987). Transonic buffet thus not only affects the aerodynamic performance but may also impose severe loads on the airframe (Benoit & Legrain, 1987). Whilst lift fluctuation, an immediate and unavoidable consequence of buffet, are unfavorable in itself, their mechanical coupling with the airframe can lead to a detrimental structural response (the so-called buffeting) and may result in serious damage to the aircraft (Crouch et al., 2008). As the buffet onset practically constrains the usable range of the flight envelope (Benoit & Legrain, 1987; Molton et al., 2013), its understanding is crucial for the aircraft design process (Crouch et al., 2019) and a prerequisite to identify and potentially shift the limits of the flight envelope. The large number of applications of supercritical airfoils increases the significance of a thorough understanding of the buffet phenomenon. With an increasing demand for fast air travel, the overall efficiency of modern civil aircraft becomes increasingly interesting. Summarizing several decades of research, Jacquin et al. (2016) characterized transonic buffet as one of the major challenges to the performance of modern civil aircraft.

Even though self-sustained unsteady shock-wave motion in the context of buffet on transonic airfoils has been explored for decades (McDevitt & Okuno, 1985; Lee, 1990), the mechanisms that initiate and maintain these self-sustained shock oscillations are still not entirely understood. Several possible explanations for the underlying mechanisms triggering this oscillatory shock motion have been suggested. The well-established model proposed by Lee (1990) and refined by Hartmann et al. (2013) captures this unsteady fluid motion based on a feedback loop. According to the model, two sequential phases of downstream and upstream propagation of disturbances form the recurring buffet cycle. The shock motion initiates pressure waves that subsequently propagate downstream to the trailing edge. Upon interacting with the latter, disturbances are emitted and travel upstream along the airfoil surface. These disturbances provide the amount of energy required to maintain the back and forth motion of the shock wave and thus close the feedback loop. Crouch et al. (2008) linked the buffet onset with a global instability of the flow, and thus contributed significantly to the perception of the phenomenon and enhanced the prediction of the buffet onset. However, variations of the chord based Reynolds number may induce significant changes both in buffet amplitude and frequency (Stanewsky & Basler, 1990). In addition, various external conditions seem to affect the buffet onset, amongst them wind-tunnel and model properties (Accorinti et al., 2021), which may render a universally-valid buffet-onset prediction impossible.

To contribute to the understanding of airfoil buffet, we discuss the shock motion and turbulence behavior for fully-developed buffet conditions in the transonic flow past the supercritical OAT15A airfoil. A broad range of buffet-relevant flow conditions for the same airfoil geometry was reported in prior investigations (Jacquin et al., 2009; Accorinti et al., 2021; Sartor et al., 2015; Nitzsche et al., 2019). Therefore, we investigated a broad parameter space in terms of incoming Mach number and geometric angle of attack in a previous investigation to clearly delineate the subspace relevant for shock buffet. Due to the suggested sensitivity of buffet to the model, wind tunnel, and flow conditions, we identified the most pronounced buffet conditions for our configuration. For these conditions, we present a detailed investigation of the flow field throughout the buffet cycle in the present study. High-speed focusing-schlieren measurements and particle-image-velocimetry (PIV) measurements were conducted to capture the shock-buffet-dominated organization of the flow. A detailed discussion of the global flow topology, the mean flow, and turbulence statistics is presented. Particular focus is on large-scale modification of the flow topology associated with periodic back and forth oscillation of the shock wave.

2. Experimental methods

In the subsequent sections we provide an overview of the experimental arrangement used for the present study. Details of the wind tunnel test section and model geometry, as well as the applied measurement techniques will be presented.

2.1. Wind tunnel facility

Our experiments were conducted in the closed-circuit Trisonic Wind Tunnel at the Institute of Aerodynamics, RWTH Aachen University. The Trisonic Wind Tunnel is an intermittently-operated vacuum-type indraft facility. Based on interchangeable test sections and adjustable nozzle geometries, it can provide Mach numbers between $0.3 < \mathrm{M}_\infty < 4.0$. Continuously run screw-type compressors evacuate a vacuum chamber with a total volume of $380\,m^3$ downstream of the test section and transport the air through a dryer bed before it enters a large $180\,m^3$ air reservoir at ambient conditions. Turnaround times of approximately 7 minutes are achieved. The relative humidity of the air is kept below 4 % to preclude condensation effects and falsification of the measured shock location (Binion, 1988). Upon initialization of a measurement cycle, a fast-acting valve is actuated, allowing the high and low pressure sections to retrieve equilibrium conditions, thus drafting the measurement medium from the balloon through the test section into the vacuum tanks. In each measurement cycle, stable flow conditions are obtained for 2 to 3 seconds, depending on the configured Mach number. The turbulence intensity based on the freestream velocity fluctuation of the wind tunnel is below 1 %. Measurements of the present campaign are performed at Mach numbers in the high subsonic regime, equivalent to transonic operation mode. The transonic test section features a rectangular cross section of 400 mm x 400 mm and a total length of 1,410 mm.

The transonic test section is equipped with flexible upper and lower walls to account for influence

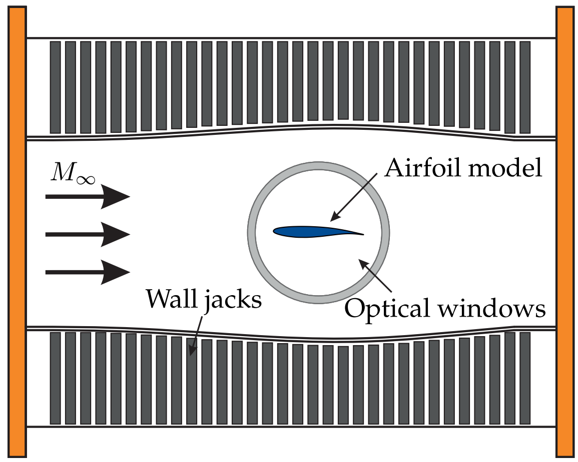

Figure 1. Illustration of the transonic test section with adjustable walls and optical access windows

of solid walls confining the flow and to emulate conditions in terms of streamline contouring observed in the equivalent free, unconfined flow around the same airfoil geometry (McDevitt et al., 1982). The schematic representation of the airfoil installed in the optically accessible test section is provided in Fig. 1. The obtainable Reynolds number is a function of the selected Mach number and the ambient conditions of the resting, predried air in the reservoir.

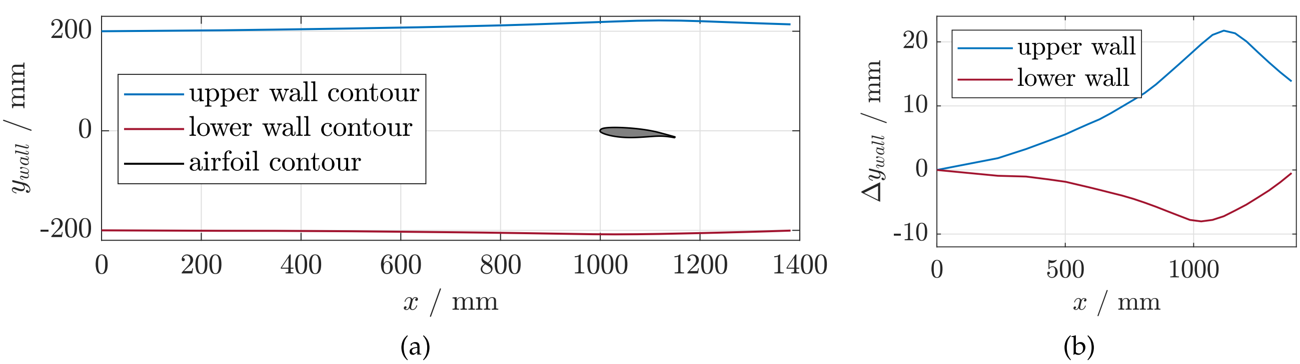

Figure 2. Wind-tunnel wall-displacement contours used for the present experiment; equal scaling illustrating the test section dimensions (a) and detailed view of the wall displacement (b).

For the present study, measurements were conducted at $\mathrm{M}_\infty = 0.72$, which is equivalent to a free-stream velocity of $u_\infty = 235$ m/s. For the investigated airfoil configuration, a chord-based Reynolds number of $Re_c = 2 \cdot 10^6$ is obtained. The dimensions of the configuration installed in the test section are provided in Fig. 2 (a); details of the wind-tunnel wall displacement at reference conditions ($M_\infty = 0.72$, AoA $= 5\,°$) are shown in Fig. 2 (b).

2.2. Supercritical airfoil model

We studied buffet on the supercritical OAT15A airfoil. The two-dimensional wind tunnel model has a relative thickness of 12.3 % and features a total span of 399 mm, which is equivalent to the width of the test section. A chord length of $c = 150\,\mathrm{mm}$ was chosen, giving an aspect ratio of approx. 2.66. The upper and lower half of the model were manufactured from stainless steel, along with a trailing edge made of metal particle-filled epoxy resin. The center of rotation for the angle of attack is located at about mid-chord of the airfoil.

2.3. Focusing schlieren setup

A focusing schlieren system inspired by Weinstein's approach (Weinstein, 1993) has been developed by the authors (Schauerte & Schreyer, 2018) (see Fig. 3) to explore flow configurations in the transonic and supersonic Mach number regimes, which are frequently accompanied by shock-wave/boundary-layer interactions and large-scale separation (Délery & Marvin, 1986).

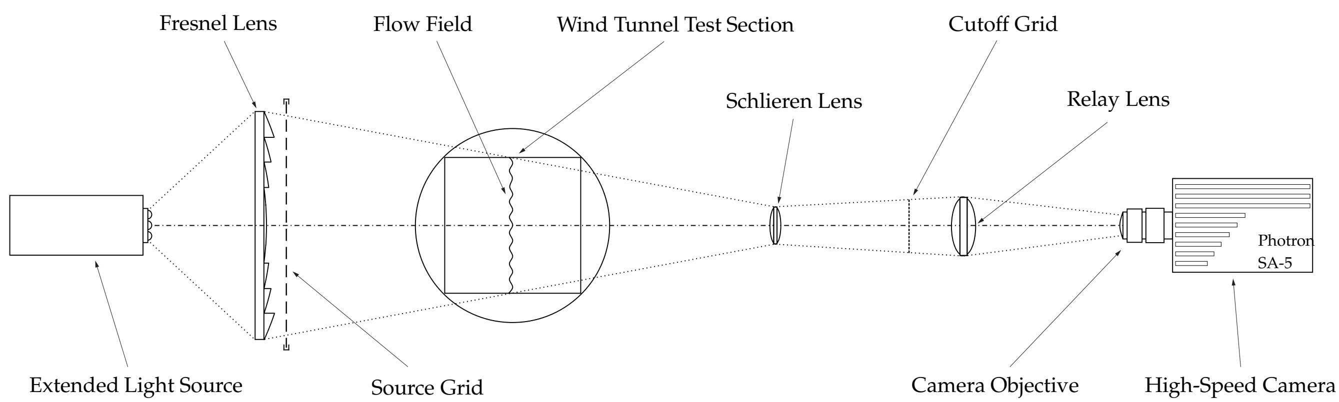

Figure 3. Schematic representation of the focusing schlieren arrangement for high-speed acquisition

Focusing schlieren overcomes some of the limitations of classical point-light-source-based schlieren configurations, including the close-to-infinite depth of focus that results in strong line-of-sight integration. The focusing capability of the system is advantageous for measurements in highly unsteady or three-dimensional flows, where fluctuating flow features and spanwise variations in topology often occur in confined slices of the flow. The setup is also capable to resolve differences in density-gradient intensity more precisely than usually obtained with parallel-light setups.

We have demonstrated (Schauerte & Schreyer, 2018) that quantitative information on the flow topology can be extracted from time-resolved schlieren-image sequences. Here, we extract the temporal development of the separation length, the shock position, as well as related frequencies of the shock oscillation. We extracted the shock location throughout the buffet cycle from a time series of focusing schlieren snapshots captured over 0.5 seconds at an acquisition rate of 20 kHz. For each snapshot, a gradient-based shock line detection was conducted at a vertical position of $0.1\,c$ above the suction side of the airfoil.

2.4. PIV measurement arrangement

To acquire detailed velocity data, we applied a particle image velocimetry (PIV) system. Planar measurements are performed in a streamwise/wall-normal plane along the centerline of the airfoil model. A Litron Nano PIV double pulsed Nd:YLF laser, operating at a wavelength of 527 nm, produces a light sheet of 1.5 mm thickness. The large laser-pulse energy of 200 mJ/pulse with a pulse duration of 4 ns ensures a high signal-to-noise ratio. The flow is seeded with di-ethyl-hexyl-sebacate (DEHS) tracer droplets with a mean diameter of 1 μm. Particle images are captured using two identical FlowSense EO 11M CCD cameras with a resolution of 11 megapixels, which corresponds to a sensor resolution of 4,008 pixels x 2,672 pixels at a pixel size of $9\ \mu m$. Both cameras are focused on the same field of view (FoV) to increase the acquisition rate to 10 Hz. The FoV covers both the shock location and the vicinity of the airfoil trailing edge. It is $145\,\mathrm{mm}$ wide and $80\,\mathrm{mm}$ high, thus spanning a streamwise domain from 0.1 c to 1.1 c. Based on the magnification of 4.04, a spatial resolution of $27.56\,\mathrm{px/mm}$ is obtained. With a final interrogation-window size of 16 px x 16 px at an overlap of 50 %, the resulting velocity maps feature a vector spacing of 0.29 mm. Relevant parameters of the focusing schlieren and PIV tests are summarized in table 1.

Table 1. Parameters of the experimental setup.

	Particle image velocimetry setup	Focusing Schlieren setup
Sensor resolution	4008 px x 2672 px	704 px x 520 px
FOV width	150 mm	180 mm
FOV height	80 mm	150 mm
Acquisition rate	10 Hz	20,000 Hz
Exposure	11 μs	1.9 μs
Spatial resolution	27.56 px/mm	4.05 px/mm
Images per case	5,300	10,000

On the basis of a phase-averaged velocity fields and turbulent quantities, we explore the governing dynamics associated with the periodic shock oscillation characterizing the buffet-dominated flow domain.

2.5. Image postprocessing and extraction of flow parameters

Based on focusing schlieren image sequences, we track the shock motion in time. With the sampling rate of 20 kHz, the large-scale shock oscillation related to buffet can be resolved faithfully. In each image (see Fig. 4), we detect the shock location at five vertical locations using an intensity-gradient-based approach. To account for AoA influences, we transform the respective coordinate system and project the obtained streamwise pixel location onto the airfoil contour. The physical coordinates, expressed in chord percentages, are computed using a spatial calibration. The thus resulting time signal of the shock location is then used to extract the upstream and downstream shock displacement defining the buffet amplitude, to compute the standard deviation of the latter, as well as to determine the temporally averaged chordwise shock location. In addition, spectral analyses were performed to identify the frequencies associated with the shock motion.

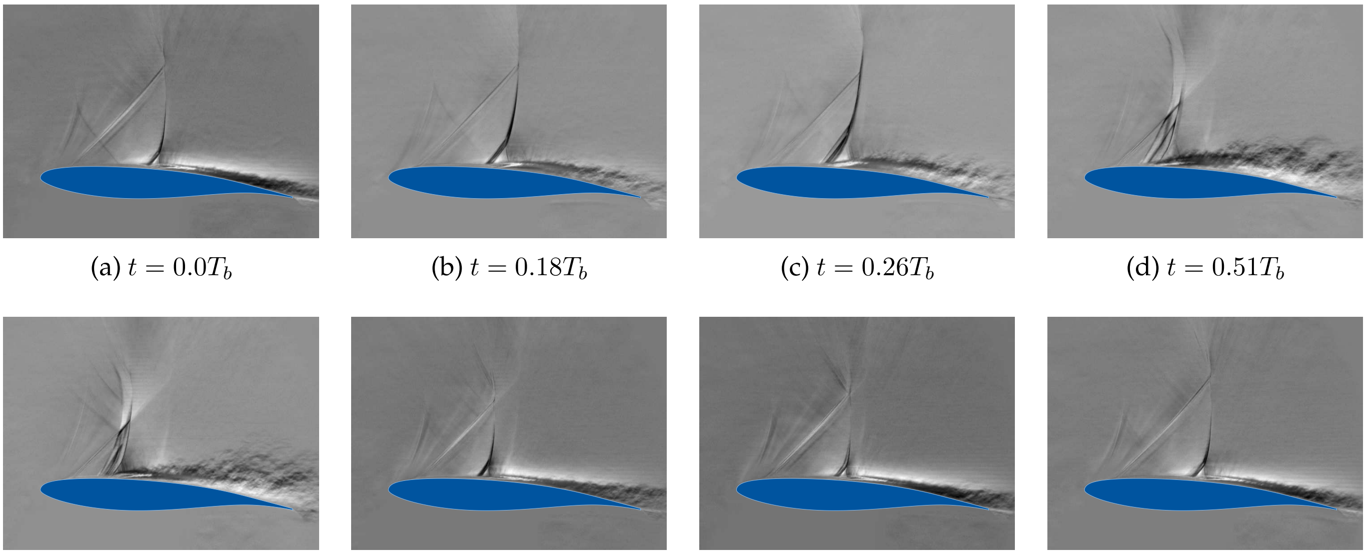

(a) $t = 0.0T_b$ (b) $t = 0.18T_b$ (c) $t = 0.26T_b$ (d) $t = 0.51T_b$

(e) $t = 0.59T_b$ (f) $t = 0.80T_b$ (g) $t = 0.87T_b$ (h) $t = 1.0T_b$

Figure 4. Characteristic focusing schlieren snapshots illustrating the shock buffet motion over one complete cycle T_b for $M = 0.72$ and $\alpha = 5°$.

Velocity fields were determined from PIV measurements. In total, 5300 temporally uncorrelated snapshots were processed. To account for the massive variation of the global flow topology throughout the buffet cycle modulated by the large-scale shock motion, we computed a phase-averaged description of the vector maps (similar to the approach discussed by D'Aguanno et al. (2021)). The snapshots were assigned to the respective bins on the basis of three criteria: the chordwise shock location, the tilt angle and shape of the shock line, as well as the post-shock streamwise velocity component u. From each instantaneous vector field, we detected the chordwise shock location at 10 vertical locations above the airfoil contour. This approach allowed to faithfully reproduce the shock line and thus to trace its modification during the buffet cycle. These three indicators allow to reliably differentiate phases of shock-upstream and shock-downstream motions and thus to sort the snapshots into their respective bins. Statistics were then computed for each bin individually. This phase-related approach provides a clear insight into the characteristic changes of the flow topology and the unique features of each buffet phase. These aspects will be discussed in terms of mean velocity contours and profiles at relevant locations in sections 3.2 and 3.3, followed by a discussion of the evolution of the turbulent wake (section 3.4).

3. Results

In the subsequent sections, we discuss results from high-speed focusing schlieren and PIV measurements to characterize the topology and turbulence behavior for airfoil buffet. First, we present and discuss the flow conditions generating the most harmonic large-scale shock oscillation, in particular regarding the key parameters characterizing fully-established shock buffet.

3.1. Characterization of the fully-established buffet cycle

Both the shock-oscillation amplitude and the relative standard deviation of the buffet amplitude were evaluated for an image sequence of 10,000 snapshots. In a preliminary study, we observed fully-developed and most stable buffet motions for a Mach number $M_\infty = 0.72$ and an incidence of $\alpha = 5°$. In addition, the latter operating conditions represent a global maximum in terms of shock amplitude and a global minimum with respect to the relative standard deviation of the amplitude. For these conditions, the 10,000 snapshots cover 57 complete buffet cycles. The time history of the shock motion during several buffet cycles is shown in Fig. 5 (a). The shock carries out a uniform sinusoidal oscillation at an almost constant amplitude of $0.165\,c$ centered around a mean shock location of $0.41\,c$. Note that the latter values denote the average amplitude evaluated over 57 complete cycles.

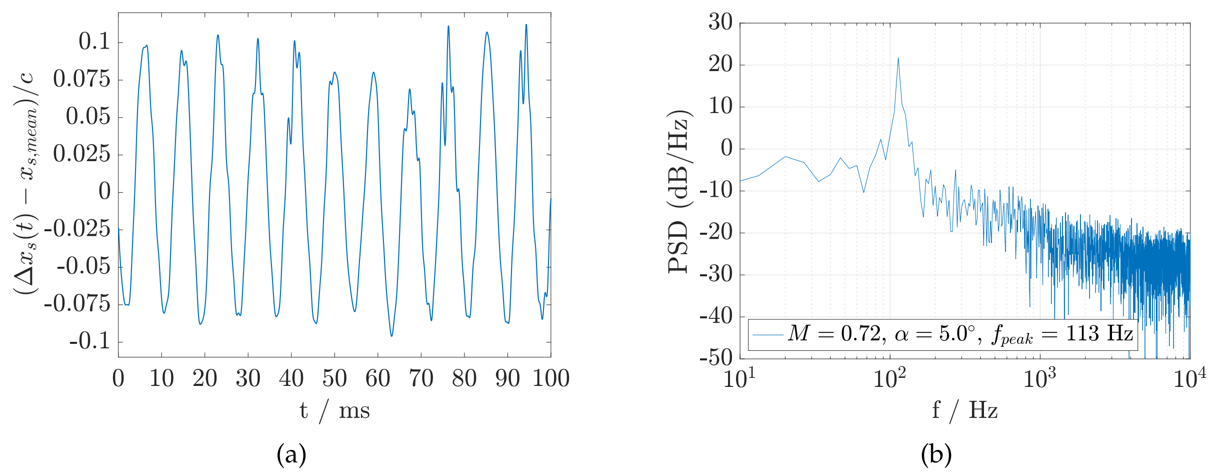

Figure 5. (a) Time trace of the chordwise shock displacement with respect to its mean position, expressed as percentage of chord; (b) Frequency spectrum related to the shock motion for $M = 0.72$ and $\alpha = 5°$.

For the time signal of the shock motion, we used an FFT analysis to compute the frequency spectrum. A dominant frequency of 113 Hz (equivalent to a chord-based Strouhal number of $St_c = 0.0714$) was identified (see Fig. 5 (b)) and clearly attributed to the large-amplitude shock oscillation illustrated in Fig. 5 (a). These findings are in good agreement with (Accorinti et al., 2021), who found an established oscillation with frequencies between $f_b = 92$ Hz and $f_b = 122$ Hz about an average shock position of $0.39\,c$ for a similar model. Similar results are found for normalized buffet frequencies: $St_c = 0.0714$ in this study, both Jacquin et al. (2009) and Schrijer et al. (2018) found $St_c = 0.067$ for the OAT15A airfoil, and Nitzsche et al. (2019) reported $St_c = 0.0716$.

3.2. Discussion of the velocity field and its variation over the buffet cycle

In this section we present velocity fields measured for the previously identified most distinct buffet condition. Instantaneous vector maps of the chordwise and vertical components are shown in Fig. 6 for three characteristic phases to provide insight into the organization of the buffet cycle and identify regions of exceptionally high turbulence intensity. Snapshots (a) and (b) represent the most upstream shock location at $x/c \approx 0.27$. Phase bin 5 (snapshots (c) and (d)) captures the shock wave at its most downstream chord position at $x/c \approx 0.49$. In addition, velocity maps indicating the final phase of the upstream motion of the shock (bin 8) are provided in snapshots (e) and (f) as they complete the buffet cycle. Note that respective u- and v-velocity maps displayed in Fig. 6 are depicted for the exact same PIV snapshot.

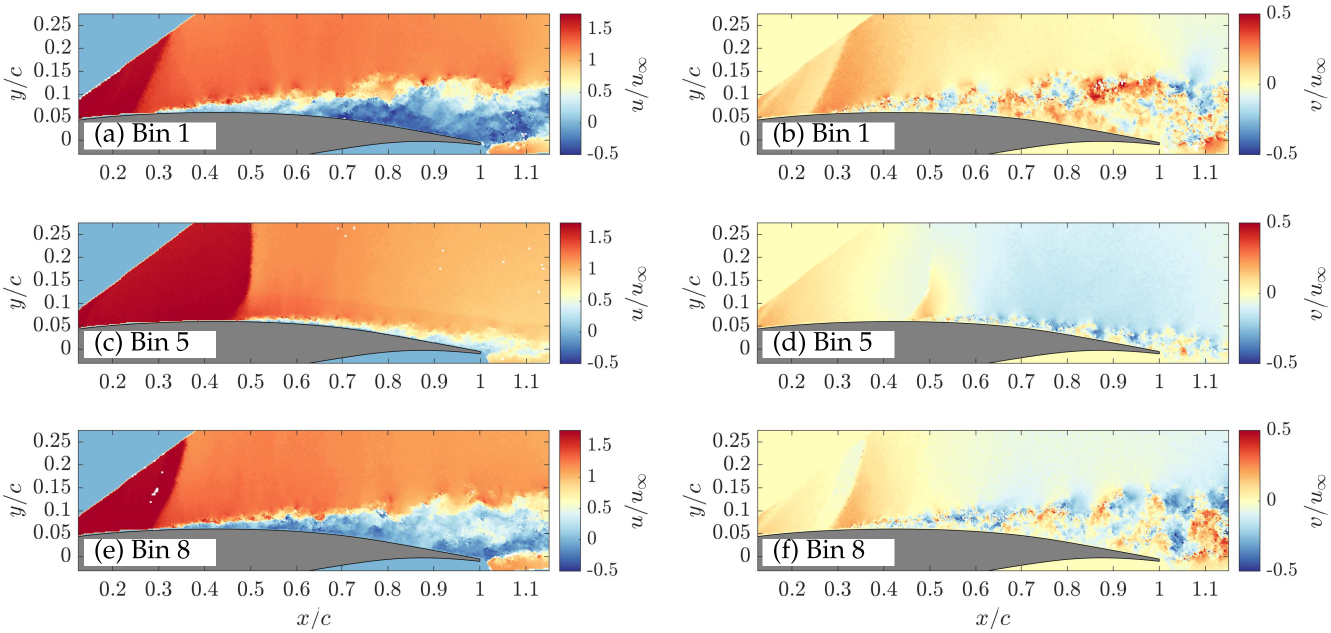

Figure 6. Instantaneous snapshots for both streamwise (u) and vertical (v) components representative for bins 1, 5, and 8.

The representative snapshots for phase bins 1, 5, and 8 in Fig. 6 underline the dynamic range inherent to both the u- and v- components in fully-established buffet mode. For the chordwise component, instantaneous magnitudes range from -0.5 u_∞ to +1.75 u_∞, and values between -0.5 u_∞ and +0.5 u_∞ were detected in the vertical component. The shock wave is reproduced as a sharp line across all depicted chordwise velocity maps and is attributed to a sudden drop in streamwise velocity, from $u \approx 404\,\mathrm{m/s}$ upstream to $u \approx 280-300\,\mathrm{m/s}$ downstream of the shock wave, depending on the respective phase. The significantly more pronounced high-velocity region downstream of the shock wave (in the λ-region) in the vertical velocity component of bins 1 and 8 highlights the upwards deflection of the flow accomodating the severe thickening of the boundary layer.

The intensity of upward displacement and the triple point location seem to be interdependent. We extracted the approximate vertical extend of the lambda region, denoted by the location of the triple point, from the instantaneous chordwise velocities (Figs. 6 (a), (c), and (e)). For the most extreme shock locations (bins 1 and 5), the vertical triple point locations are greatly different: $y/c = 0.2$ and $y/c = 0.025$, respectively. While in phase bin 1 (Fig. 6 (b)), $v \geq 0$ across the entire vertically captured region, contributions of the vertical component in bin 5 are confined to a narrow region in the direct vicinity of the shock foot (Fig. 6 (d)). The upwards deflection of the flow reduces gradually with downstream-moving chord location of the shock wave, and finally vanishes almost completely in bin 5 when the shock wave occupies its most downstream location.

The state and chordwise location of the buffet shock also allows to quantify the coupled evolution of the wake size. The pronounced vertical displacement effect of the flapping wake is most distinct in bin 1 (Fig. 6 (b)) where a slight upward deflection is visible downstream of the shock wave and above the wake. This behavior is related to an excessive thickening and subsequent separation of the boundary layer in that phase. A large wake is also observed in phase bin 8, but at reduced vertical displacement. The vertical velocity thus almost vanishes between $x/c = 0.5$ and $x/c = 0.7$ (see Fig. 6 (f)). In contrast, phase bin 5 shows a significant negative v-component downstream of the shock wave above the wake. Overall, the highly turbulent nature of the wake region is clearly visible in the turbulent structures of the v-component of bins 1, and 8 (Figs. 6 (b) and (f)).

Phase bin 1 is associated with far upstream shock locations and shows massive flow separation (see Figs. 6 (a) and (b)) induced by a shock wave that is substantially oblique. The boundary layer strongly thickens and subsequently separates downstream of the shock foot. It then strongly grows from a chord location of approximately $x/c = 0.5$ onwards. As a result, a region of highly turbulent flow spreads over the entire airfoil suction side and into the downstream wake.

Upon incipient downstream motion of the shock wave, the turbulent wake continuously decreases until it reaches its minimum extent in bin 5. Here, it is confined to a narrow band following the airfoil contour, thus indicating attached flow. Phase bin 5 shows the shock wave at its downstream reversal point, i.e. at its most extreme downstream location. The shock wave now has an exact normal shape with a triple point close to the surface.

After passing through the downstream reversal point, the shock wave becomes increasingly oblique again, which is most clearly visible in phase bin 8, which denotes the final phase of shock upstream motion. Compared with bin 1, the shock line is less oblique and the vertical extent of the turbulent wake is slightly less pronounced.

3.3. Properties of phase-averaged velocity fields

The phase-averaged velocity maps with superimposed phase-averaged velocity profiles shown in Fig. 7 give insight into the distribution of momentum and its evolution over the different phases of the buffet cycle.

The mean chordwise velocity maps of bins 1 and 8 reveal a large turbulent wake and wake-induced momentum deficit (u-component). Close to the airfoil contour, values $du/dy \leq 0$ extend throughout the entire wake along the airfoil suction side, and are noticeable until the trailing edge (TE) location, thus emphasizing the latter observation. Also the strong displacement of the wake that results in an upward deflection of the flow is nicely captured in Fig. 7 (b) for bin 1, and is weakly discernible in bin 8 (Fig. 7 (p)), both at $x/c = 0.6$. The earlier observation of an almost vanishing vertical velocity component in bins 2 and 8 is substantiated here (see Figs. 7 (d) and (p)) as the phase-averaged velocity takes values close to zero between $x/c = 0.6$ and $x/c = 0.8$ outside of the

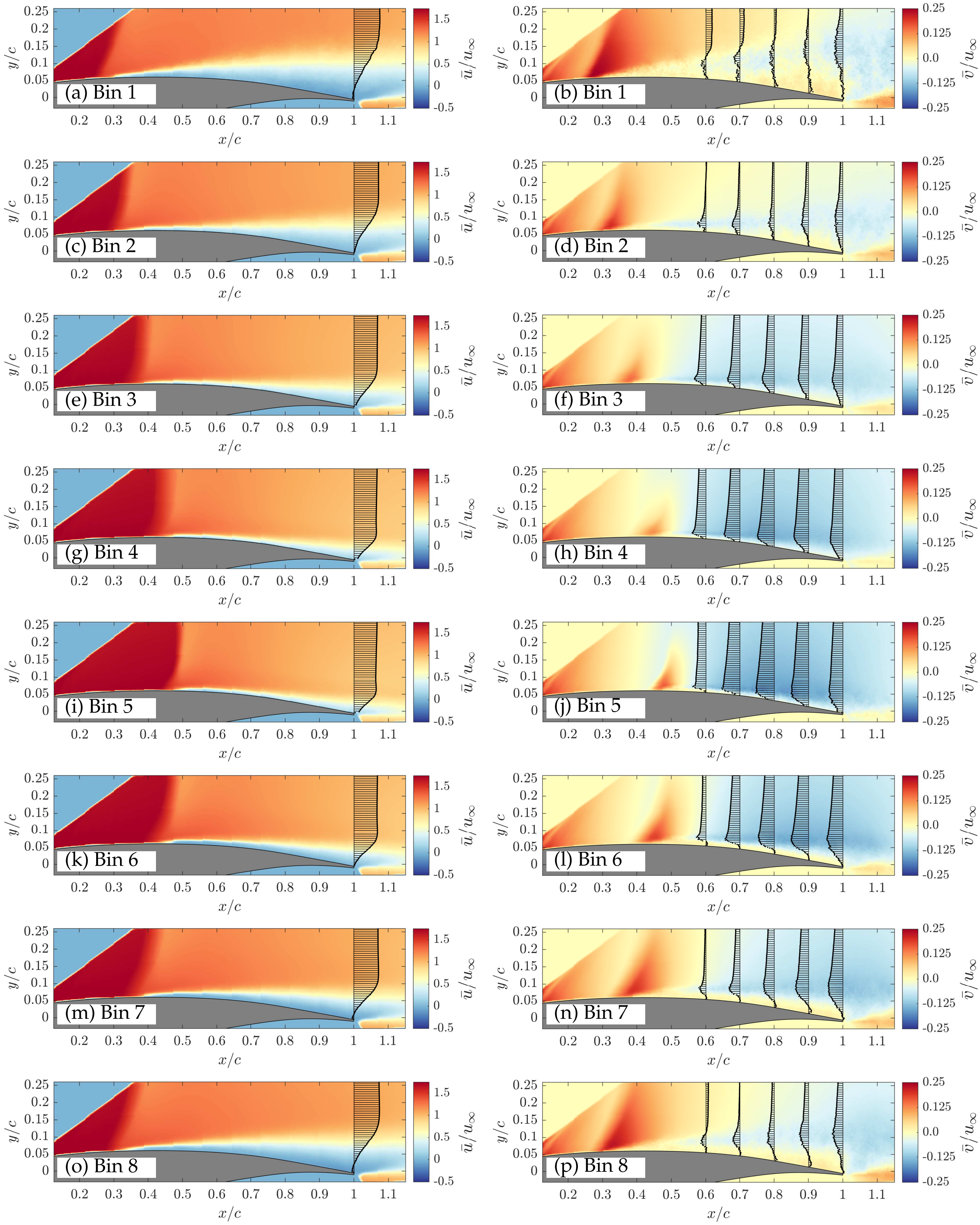

Figure 7. Phase-averaged chordwise (u-component) and vertical (v-component) velocity fields for phase bins 1 to 4.

wake.

The continued downstream displacement of the shock wave between bins 2 and 4 is accompanied by a further contraction of the turbulent wake, most apparent in the much fuller velocity profile close to the wall at $x/c = 1.0$ (see Fig. 7 (c), (e), and (g)).

As for the most upstream location in bin 1, the shock wave needs to decelerate strongly before it reaches the inverse point in bin 5. Thus, no significant shock displacement is detected in the phase-averaged map. The shape of the shock line is now exactly normal, and the λ-region has reached its minimal extent. The flow is completely attached in phase bin 5 all along the suction side, and the wake influence is only noticeable in the immediate vicinity of the airfoil contour.

Incipient upstream motion (phase bin 6) is accompanied by a steadily increasing wake influence and noticeable obliqueness of the shock line. While traveling upstream (bins 6 to 8), the shock-induced velocity deficit in u is notably smaller than in corresponding (downstream) bins 2, 3, and 4. This behavior results in greater maximum u values far away from the wall (see Figs. 7 (k), (m), and (o)). While the velocity profile of bin 6 is significantly less full than in the fully-recovered phase bin 5, bin 7 is again characterized by a largely increased wake with negative $\overline{u}$ extending until the TE. The phase-averaged chordwise velocity contours and profiles in the left column of Fig. 7 show qualitatively good agreement with Schrijer et al. (2018) regarding the shock-induced momentum deficit in the wake, even though absolute shock displacement and mean shock location seem to be different in the present case. This deviation is most probably related to substantially different model dimensions, Reynolds number, and wind tunnel characteristics.

3.4. Shock-induced flow separation and development of the turbulent wake

Details of the velocity contours and the phase-averaged velocity profiles in the vicinity of the TE are shown in Figs. 8 and 9, respectively, between $x/c = 0.9$ and $x/c = 1.1$. This region is revealing in several aspects: it illustrates the interaction of suction and pressure sides as they coalesce at the TE and also provides an estimate of the influence of the turbulent wake downstream of the airfoil.

The detailed view of the phase-averaged u-component at the TE region (Fig. 8) allows to track the vertical extent of low-momentum wake, as well as the transition of the shear layer into the external flow field. As expected from the global flow topology (see Fig. 7), largest momentum deficits occur for phases of far upstream shock locations, and are thus most distinct in bin 1. The phase-averaged velocity profile $\overline{u}(x/c = 1)$ at the TE further reveals that the low-momentum wake stretches far into the external flow field. The shear layer influence is thus significant up to $y/c = 0.15$ (see Fig. 8 (a)). A portion of reverse flow persists until the TE location and is only compensated by the coalescence of the both flow fields from the suction and pressure side downstream of the TE. Negative $\overline{u}$ extend up to $\Delta y/c \approx 0.04$ above the TE – this denotes the largest contribution of reverse flow across all bins. The velocity profile is the least full of all phases and seems to recover completely only after $y/c = 0.2$, where it assumes values close to the free stream velocity.

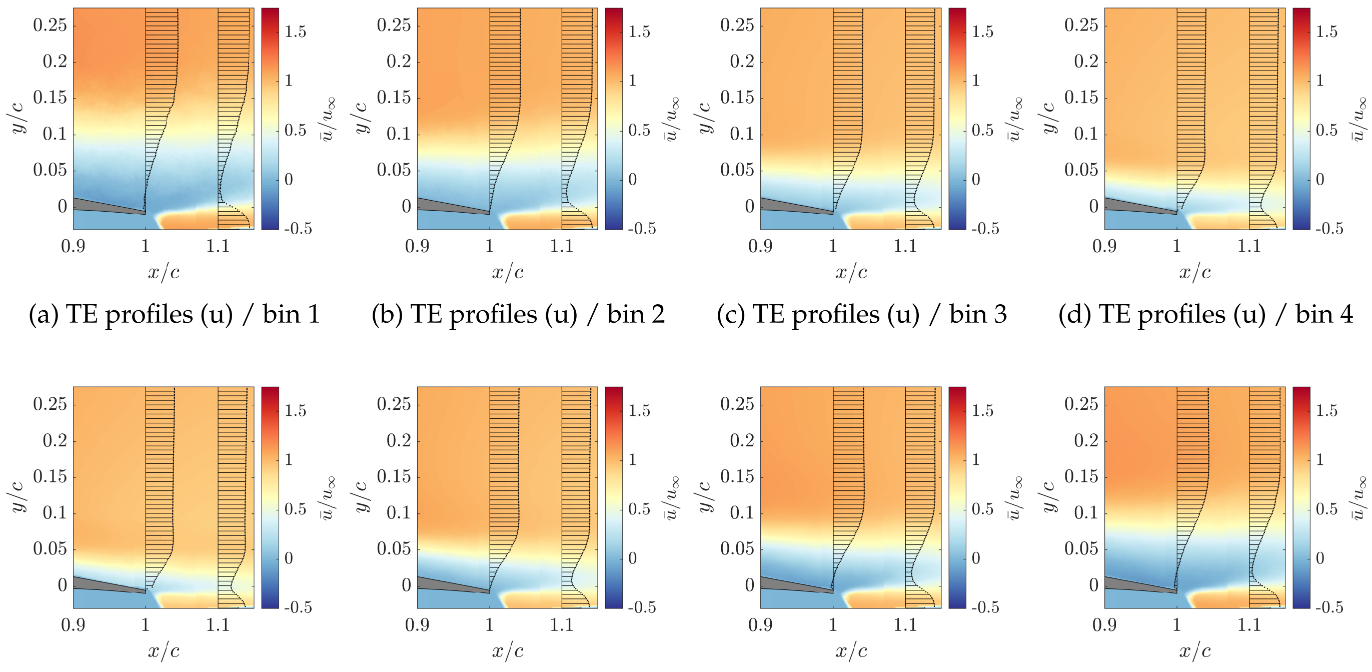

(a) TE profiles (u) / bin 1 (b) TE profiles (u) / bin 2 (c) TE profiles (u) / bin 3 (d) TE profiles (u) / bin 4

(e) TE profiles (u) / bin 5 (f) TE profiles (u) / bin 6 (g) TE profiles (u) / bin 7 (h) TE profiles (u) / bin 8

Figure 8. Phase-averaged velocity profiles (u-component) at the TE (x/c=1.0) and near wake region (x/c=1.1).

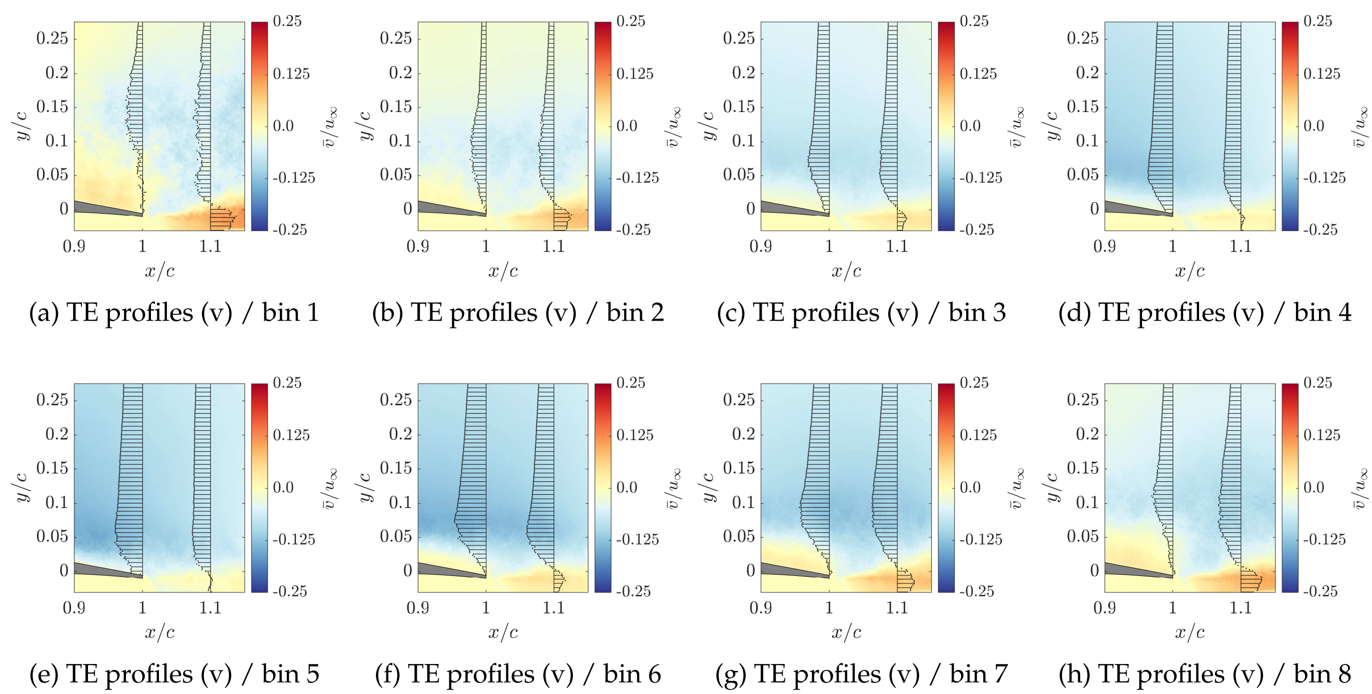

(a) TE profiles (v) / bin 1 (b) TE profiles (v) / bin 2 (c) TE profiles (v) / bin 3 (d) TE profiles (v) / bin 4

(e) TE profiles (v) / bin 5 (f) TE profiles (v) / bin 6 (g) TE profiles (v) / bin 7 (h) TE profiles (v) / bin 8

Figure 9. Phase-averaged velocity profiles (v-component) at the TE (x/c=1.0) and near wake region (x/c=1.1).

Note that in phases with massive flow separation, the velocity profiles converge to larger values towards the freestream (compare Figs. 8 (a) and (e)). This behavior is related to the displacement effect of the low-momentum region, as discussed in section 3.3.

In the mean wake profiles of subsequent bins, the low-momentum cone-shaped region in the mixing zone between $x/c = 1.0$ and $x/c = 1.1$ decreases steadily with increasing downstream location of the shock. The velocity profile starts to recover in bin 2 in that the vertical extent of the wake and its related momentum deficit has reduced compared with bin 1. This tendency is underlined by regained momentum and consistently positive streamwise velocities.

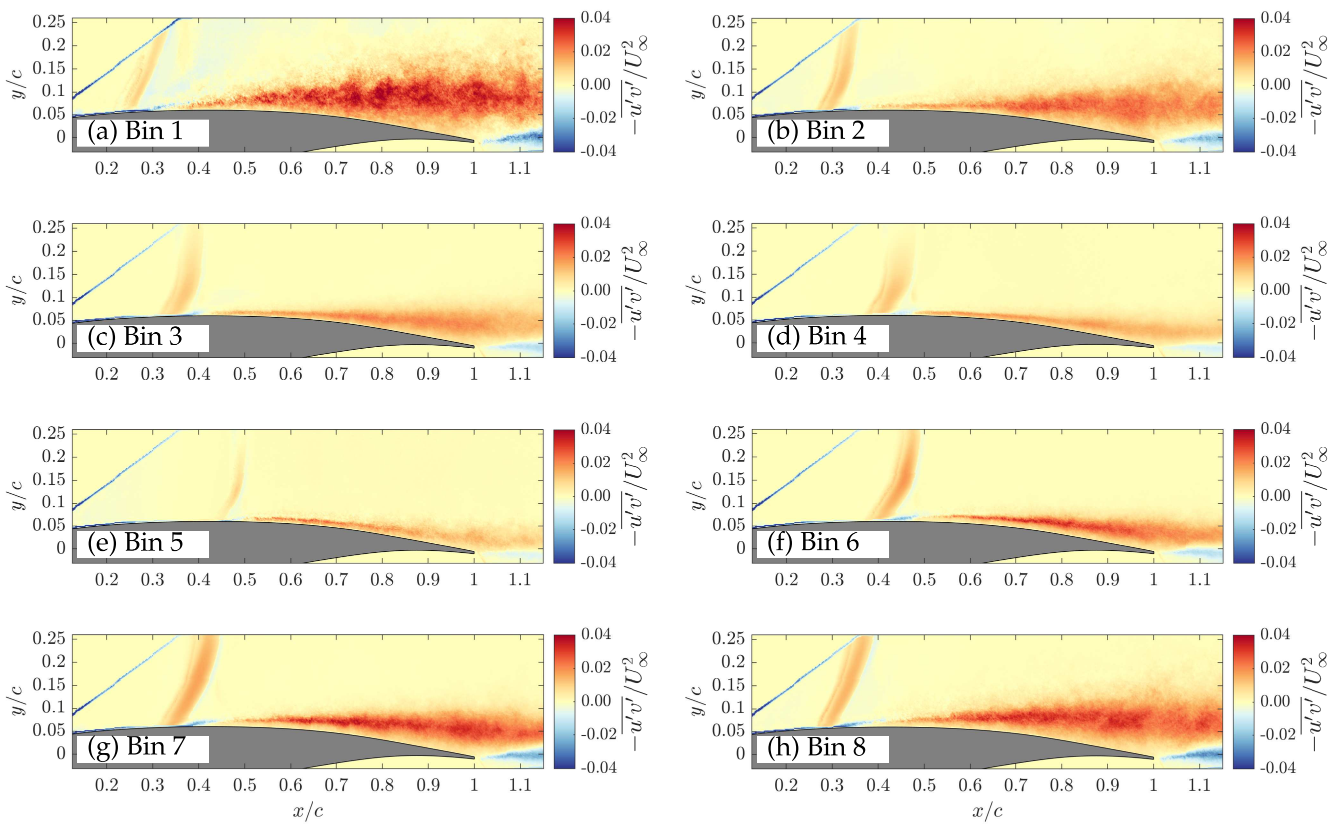

Figure 10. Reynolds shear stress distribution for all phase bins.

The momentum deficit has widely recovered when the shock wave reaches its most downstream position (bin 5). Subsequently, in the transition from downstream to upstream shock motion, the boundary layer significantly thickens and the wake region grows steadily (see sequence of bins 6, 7, and 8 in Figs. 8 (f), (g), and (h)). The vertical distance of the shear layer from the trailing edge point indicates the separation strength and thus the wake intensity. These results clearly illustrate the large variation in the near-wake development throughout a buffet cycle.

In the velocity contours in Figs. 8 and 9, a sharp separation line between regions of high and low momentum, i.e. freestream and wake, is observed. In particular downstream of the TE, this transition occurs along a characteristic line both on the upper and lower sides of the wake. In the sequence from bin 1 to bin 8, we observe unique angles denoting the separation line that confines the wake expansion downstream of the TE. While the pressure-side flow is clearly shifted upwards in bins 1, 2, 7, and 8, the line is almost horizonal for bins 4 and 5 (Fig. 9 (d) and (e)), which is emphasized by a vertical velocity close to zero. These observations indicate that the flow fields on both suction and pressure sides are coupled by a common downstream angle as they coalesce at the trailing edge. The influence of the suction side seems to be dominating here.

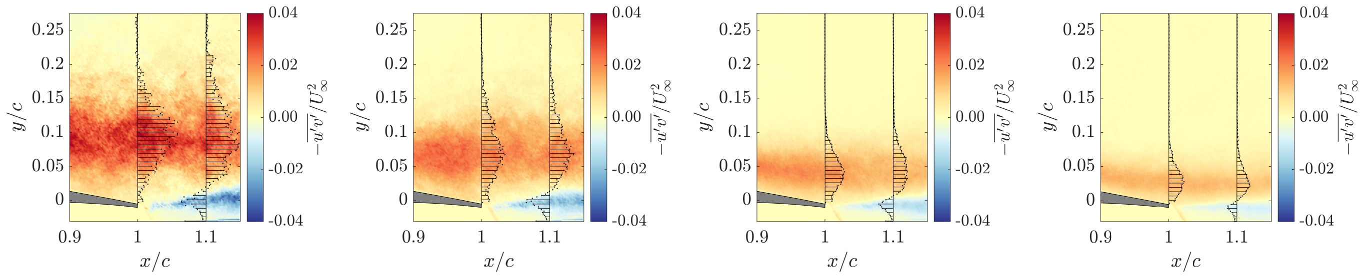

(a) Phase bin 1 (b) Phase bin 2 (c) Phase bin 3 (d) Phase bin 4

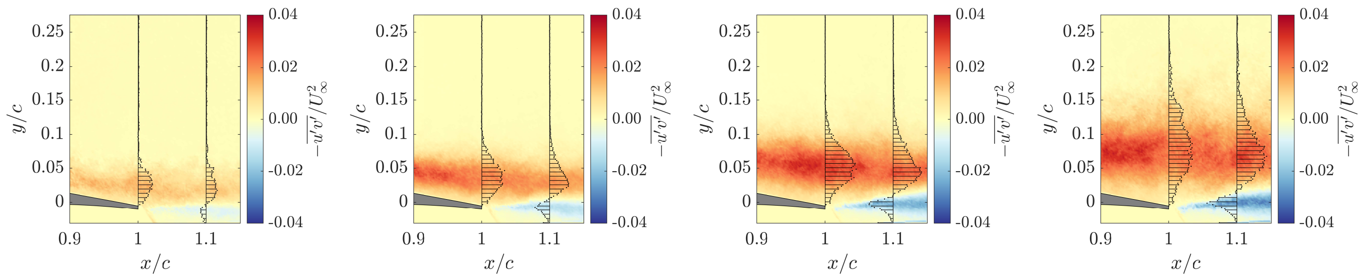

(e) Phase bin 5 (f) Phase bin 6 (g) Phase bin 7 (h) Phase bin 8

Figure 11. Details of the Reynolds shear stress distribution at the TE (x/c=1.0) and near wake region (x/c=1.1) for all phase bins.

The Reynolds shear-stress maps in Fig. 10 are in accordance with the findings discussed on the basis of Fig. 6: incidents of large-scale flow separation are governed by intense turbulent mixing, as is most clearly represented by snapshots (a) and (o) of Fig. 6. These findings are reproduced in the shear stress contributions of bin 1 (see Fig. 11 (a)) and bin 8 (see Fig. 11 (h)), whose maximum is located far above the TE at $y/c = 0.1$ (bin 1) and $y/c = 0.075$ (bin 8), whereas the wake influence is still noticeable until $y/c = 0.2$ in both phases of the buffet cycle. Greatest maximum shear stress values are attributed to phase bin 1, which confirms the qualitative observations of the instantaneous vector field in Figs. 6 (a) and (b). In contrast, bin 5 expectedly shows the weakest shear stress with a vertical peak location at $y/c = 0.025$. This immense variation within the buffet cycle further illustrates the strong flapping motion of the wake.

Note that the shear stress contribution converges towards zero above the wake, which underlines the low level of turbulence in the external flow initially reported for all snapshots in Fig. 6. The strong coupling between the airfoil suction and pressure side wakes discussed above is reflected here in the synchronized increase and decrease of the positive (upper side) and negative (lower side) shear-stress contribution over the different phases. More precisely, the absolute magnitude of Reynolds stresses (either positive or negative), as well as their vertical extent are largest when the shock is located upstream, and shrink consistently with increasing chordwise location x/c. Even in phases where the shock wave travels downstream and the flow is fully attached, the Reynolds shear stress at the TE is not equal to zero. This observation indicates a non-negligible amount of turbulence imposed by the buffet shock. Overall, these results confirm and further illustrate the findings presented in sections 3.2 and 3.3.

4. Conclusions

The buffet phenomenon on the 2D supercritical OAT15A airfoil was investigated experimentally by means of high-speed focusing schlieren and PIV measurements. The airfoil suction side was captured from $x/c = 0.1$ to $x/c = 1.1$. For flow conditions generating fully-established shock buffet, centered around $M_\infty = 0.72$ and $\alpha = 5\,°$, the flow topology, turbulence behavior, and shock motion were analyzed in detail. A fully harmonic oscillatory shock motion at a unique buffet frequency of 113 Hz ($St_c = 0.0714$) was observed, and the shock amplitude spanned a range of $16.5\,\%$ of the airfoil chord. We demonstrated that large-scale oscillations of the shock wave initiate strong variations of the flow topology. The associated large variation of shock-induced recompression causes a periodic modulation of the flow separation that is most notably governed by a massive flapping motion of the turbulent wake. Incidents of massive flow separation are only observed for shock positions close to the upstream limit (bins 1 and 8), and the wake influence is most pronounced when induced by an upstream traveling shock wave. A unique set of velocity profiles describes each phase of the buffet cycle, which emphasizes the severe global modification of the flow topology modulated by the upstream and downstream moving shock wave. These variations have a substantial effect on the state of the boundary layer. Phases of most upstream shock locations are subject to pronounced flow separation that extends until the airfoil trailing edge, whereas fully-recovered attached flow is observed for most downstream shock locations.

Acknowledgements

The authors gratefully acknowledge the Deutsche Forschungsgemeinschaft DFG (German Research Foundation) for funding this work in the framework of the research unit FOR 2895. The authors wish to thank ONERA for providing the OAT15A airfoil geometry that was used to manufacture the wind tunnel model. We also gratefully acknowledge the contribution and support of Nick Capellmann and the entire workshop team of the Institute of Aerodynamics during the manufacturing process of the wind tunnel model.

Nomenclature

α	Airfoil angle of attack [deg]
δ_0	Thickness of the incoming turbulent boundary layer [mm]
σ_{A_s}	Relative standard deviation of shock amplitude
c	Chord length of airfoil [mm]
M	Mach number [-]

M_∞	Mach number of the incoming flow [-]
Re_c	Reynolds number based on the airfoil chord length [-]
St_c	Strouhal number based on the airfoil chord length [-]
T_b	Duration of a complete buffet cycle [s]
u_∞	Freestream velocity [m/s]
x	Longitudinal (streamwise) coordinate [mm]
x_s	Chordwise shock location [mm]
Δx_s	Chordwise shock displacement [mm]
$\bar{x}_s$	Mean streamwise shock location [mm]
y	Vertical coordinate [mm]
AoA	Angle of attack
DMD	Dynamic mode decomposition
FOV	Field of view
PIV	Particle image velocimetry
SBLI	Shock-wave/boundary layer interaction
TE	Trailing edge

References

Accorinti, A., Baur, T., Scharnowski, S., Knebusch, J., Dillinger, J. K. S., Govers, Y., ... Kähler, C. J. (2021). Measurements of deformation, schlieren and forces on an oat15a airfoil at pre-buffet and buffet conditions. *IOP Conference Series: Materials Science and Engineering*, *1024*.

Benoit, B., & Legrain, I. (1987). Buffeting prediction for transport aircraft applications based on unsteady pressure measurements. *AIAA 5th Applied Aerodynamics Conference*.

Binion, T. W. (1988). Potentials for pseudo-reynolds number effects. *AGARDograph*, *303*.

Crouch, J., Garbaruk, A., Magidov, D., & Travin, A. (2008). Origin and structure of transonic buffet on airfoils. *5th AIAA Theoretical Fluid Mechanics Conference*.

Crouch, J., Garbaruk, A., & Strelets, M. (2019, oct). Global instability in the onset of transonic-wing buffet. *Journal of Fluid Mechanics*, *881*, 3–22.

D'Aguanno, A., Schrijer, F. F. J., & van Oudheusden, B. W. (2021, oct). Experimental investigation of the transonic buffet cycle on a supercritical airfoil. *Experiments in Fluids*, *62*(10).

Délery, J., & Marvin, J. (1986). Shock-wave boundary layer interactions. *AGARDograph*, *280*.

Hartmann, A., Feldhusen, A., & Schröder, W. (2013). On the interaction of shock waves and sound waves in transonic buffet flow. *Physics of Fluids*, *25*(2).

Jacquin, L., Brion, V., Molton, P., Sipp, D., Dandois, J., Deck, S., ... Caruana, D. (2016, December). Testing in aerodynamics research at onera: the example of the transonic buffet. *AerospaceLab*, *12*.

Jacquin, L., Molton, P., Deck, S., Maury, B., & Soulevant, D. (2009). Experimental study of shock oscillation over a transonic supercritical profile. *AIAA Journal*, *47*(9), 1985-1994.

Lee, B. H. K. (1990). Oscillatory shock motion caused by transonic shock boundary-layer interaction. *AIAA Journal*, *28*(5), 942-944.

McDevitt, J. B., & Okuno, A. F. (1985, June). Static and dynamic pressure measurements on a naca 0012 airfoil in the ames high reynolds number facility. *NASA Technical Paper 2485*.

McDevitt, J. B., Polek, T., & Hand, L. (1982). A new facility and technique for two-dimensional aerodynamic testing. *12th Aerodynamic Testing Conference*.

Molton, P., Dandois, J., Lepage, A., Brunet, V., & Bur, R. (2013). Control of buffet phenomenon on a transonic swept wing. *AIAA Journal*, *51*(4), 761-772.

Nitzsche, J., Ringel, L. M., Kaiser, C., & Hennings, H. (2019). Fluid-mode flutter in plane transonic flows. *IFASD 2019 – International Forum on Aeroelasticity and Structural Dynamics*.

Sartor, F., Mettot, C., & Sipp, D. (2015, 07). Stability, receptivity, and sensitivity analyses of buffeting transonic flow over a profile. *AIAA Journal*, *53*, 1980-1993.

Schauerte, C., & Schreyer, A.-M. (2018, July). Design of a high-speed focusing schlieren system for complex three-dimensional flows. *5th International Conference on Experimental Fluid Mechanics ICEFM 2018 Munich*.

Schrijer, F., Solana Perez, R., & van Oudheusden, B. (2018, July). Investigation of transonic buffet using high speed piv. *5th International Conference on Experimental Fluid Mechanics ICEFM 2018 Munich*.

Stanewsky, E., & Basler, D. B. (1990). Experimental investigation of buffet onset and penetration on a supercritical airfoil at transonic speeds. *AGARD Conference Proceedings*, *483*.

Weinstein, L. M. (1993). Large-field high-brightness focusing schlieren system. *AIAA Journal*, *31*(7), 1250-1255.